Research article

Effect of assembly pressure on the performance of proton exchange membrane fuel cell

Zhuo Zhang, Wen-Quan Tao*

Key Laboratory of Thermo-Fluid Science & Engineering of MOE, Xi'an Jiaotong University, Xi'an, 710049, China

ABSTRACT

The assembly force is a crucial factor in the process of proton exchange membrane fuel cell (PEMFC) stacking, and has significant effects on the fluid flow, mass transfer, and water and thermal management, which affect the fuel cell performance. In this study, from the most deformable component, the gas diffusion layer (GDL), combining with a finite-element analysis, and computational fluid dynamic method, the impact of the assembly force on a single-channel PEMFC is analyzed. A nonlinear stress–strain curve obtained from a microanalysis is creatively introduced into the two-dimensional compression model. The gas diffusion coefficient in the three-dimensional model is also obtained from the microscopic simulation. The simulated effective oxygen diffusion coefficient of the compressed GDL is approximately 0.86 times the Bruggemann estimated value. When the contact resistance is ignored, the output voltage at 2.5 MPa is decreased by approximately 15.4% at 1.7 A·cm^{-2} compared with that at 0.5 MPa. After the contact resistance is considered, the effects of the assembly pressure on the cell performance (V–I curve) are qualitatively different. The pressure drop of the 2.5 MPa case is 20% higher than that of the 1.4 MPa case at 1.7 A cm^{-2}. O_2 is hard to flow into the region under the rib where the porosity and permeability are lower. The results indicate that both liquid water and membrane water contents increase when the assembly force increases. The effect of the assembly force on the temperature is also analyzed.

1. Introduction

With the increase in energy consumption, more efficient and environmentally friendly energy resources are required worldwide [1,2]. Proton exchange membrane fuel cell (PEMFC) is an energy conversion device that directly converts hydrogen to electricity. Recently, it has attracted an increasing interest due to its high power density, high efficiency, and rapid startup [3]. The membrane electrode assembly (MEA) is the core of the fuel cell, which consists of a PEM sandwiched symmetrically with catalyst layers (CLs), microporous layers (MPLs), and gas diffusion layers (GDLs). A bipolar plate (BP) or flow field plate is responsible for reactant supply, product removal, structure support, and electricity collection. An MEA is sandwiched between the anode and cathode BP to form a single cell. In commercial applications, usually over hundreds of single cells need to be assembled into a stack to satisfy the power requirement [4]. The assembly force is also important for gas sealing and reduction in the contact resistance. When the assembly force is too small, hydrogen leakage causes safety hazards, and the contact resistance increases, which reduces the cell performance [5]. However, an excessive force reduces the porosity in the GDL, resulting in a deterioration of mass transfer in the porous electrode. Chen and

Su [6] experimentally studied the effects of the assembly torque on the PEMFC performance. The performance of the PEMFC increased by approximately 21% as the torque increased from 2 to 6 N·m. However, the performance decreased by approximately 11% as the torque further increased from 6 to 7 N·m due to decreases in GDL porosity and hydrophobicity, and deformation of the flow channel in the stamped metallic BP. In this regard, it is highly required to study the effect of the assembly pressure on the performance of the PEMFC.

With the lowest elastic modules among the components of the MEA, the GDL undergoes a large and inhomogenous deformation under the assembly force compared with other components such as the MPL and CL. Extensive studies have been carried out on the mechanical behavior of GDL compression. Ismail et al. [7] experimentally investigated the mechanical behavior under a compression for several GDLs. Keller et al. [8] employed an optical measurement method to evaluate the influences of channel parameters on the intrusion behavior of GDLs under preload conditions. The intrusion of a GDL into the cross-sectional area of a channel structure is fundamentally dependent on the channel parameters, such as the channel width and channel-to-rib ratio. Baik et al. [9] elucidated the correlation between the anisotropic bending stiffness of a GDL and land/channel width ratio of the metal BP. Carrel and Mélé [10] proposed an approach using stress–relative density curves rather than traditional stress–strain curves to analyze the mechanical behavior of carbon papers. Serincan and Pasaogullari [11] and Lu et al. [12] investigated the effects of GDL anisotropy on the stress distribution in

Nomenclature

a, b, c	Constant coefficients
C	Gas concentration, mol·m^{-3}
D	Gas diffusivity, m^2·s^{-1}
E	Young's modulus, Pa
R	Electrical contact resistance, mΩ
S	Area of contact element, cm^2
f	Correction factor
s_{lq}	Liquid water saturation

Greek letters

κ	Permeability, m^2
γ	Porosity
α	Phase change rate, s^{-1}
ρ	Density, kg·m^{-3}
σ	Electrical conductivity, S·m^{-1}
τ	Tortuosity
δ	Thickness, mm

Subscripts and superscripts

0	Intrinsic
ACL	Anode catalyst layer
BP	Bipolar plate
CCL	Cathode catalyst layer
CGDL	Cathode gas diffusion layer
CMPL	Cathode microporous layer
GC	Gas channel
GDL	Gas diffusion layer
MEM	Membrane
MPL	Microporous layer
eff	Effective
m	Simulated

Fig. 1. Constructed model and boundary conditions [13]. (a) Isometric view of the constructed model; (b) side view of the constructed model and applied boundary conditions.

a PEMFC with a finite-element model. In our previous study [13], the nonlinear stress–strain relationship of the GDL was analyzed based on the fiber matrix microstructure. The effects of the porosity, carbon fiber diameter, and thickness on the mechanical behavior were analyzed.

The compression inevitably affects the water and gas transport in the GDL. Froning et al. [14] simulated the gas transport in nonwoven-type GDLs using the lattice Boltzmann method. The effective permeability κ_{eff} and tortuosity τ were calculated by through- and in-plane transport simulations. Xu et al. [15] developed an integrated model to predict the water transport in a nonuniformly compressed GDL. The drainage pressure increased monotonically with the assembly clamping force. Quantitative relationships between effective properties (gas diffusivity and permeability) for a dry GDL and corresponding microstructure characteristics have been established by Holzer et al. [16]. The variation in gas diffusivity with the compression has been related mainly to changes in porosity and geodesic tortuosity. In addition to the mass transport, the thermal and electrical conductivities of the GDL are also affected by the compression. Chowdhury et al. [17] and Sadeghi et al. [18] measured the GDL bulk thermal conductivity under an inhomogeneous compression. The effective conductivity increases with the compressive load due to the larger size and number of contacts between the fibers. A systematic experiment was carried out by Qiu et al. [19] to investigate the electrical resistances and microstructures of commonly used GDLs (carbon paper, carbon cloth, and carbon felt) under cyclic and steady loads. The felt GDL had the lowest electrical conductivity. Its tortuous and thick fibers contributed to a higher stability in terms of electrical resistance and microstructure under a compression than those of a bonded carbon paper and woven carbon cloth.

The change in the GDL properties further affects the cell performance. By experiments, Uzundurukan et al. [20] analyzed the bolt and clamping plate compressions under various loads, and the maximum
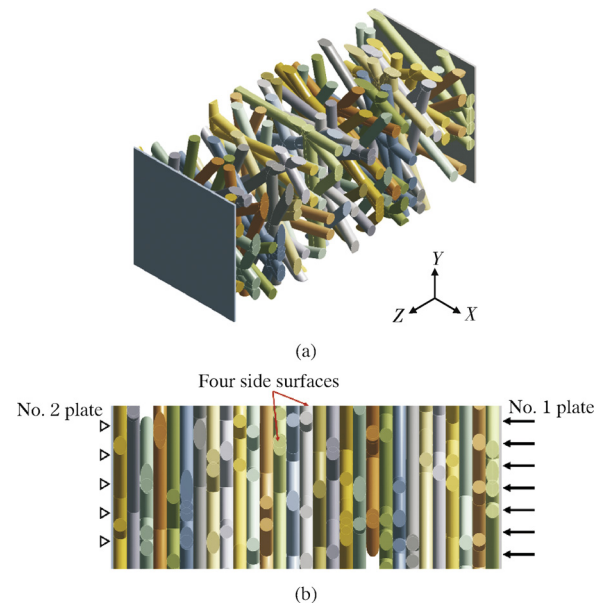
power densities were compared. In addition to experiments, numerical simulations have been carried out to study the effect of the assembly pressure on the cell performance [21,22]. As described above, the compression directly affects the GDL. Therefore, The GDL deformation and property change should be carefully and comprehensively considered in the model. Many researchers obtain the GDL compressed profile by a finite-element method (FEM) simulation, and then import it into the three-dimensional (3D) multiphase computational fluid dynamics (CFD) model [23,24]. However, in the above studies, the constant Young's modules have been employed to calculate the GDL deformation during the FEM simulation, which cannot reflect the nonlinear stress–strain mechanical behavior. Among several transport properties of the GDL, the gas diffusivity is a crucial parameter that influences the mass transport, considering that the diffusion is the primary mass transfer mechanism in the GDL. The traditional Bruggemann correction (power of porosity of 1.5), a macroscopic approximation, is widely used to calculate the effective gas diffusivity. In this method, the diffusivity is dependent only on the porosity. A more accurate and reasonable diffusivity should be obtained through a simulation based on the microstructure.

In this study, the nonlinear stress–strain curve of a paper-type GDL is introduced into the FEM simulation to obtain the compressed GDL profile. Based on the compressed GDL microstructure obtained in our previous study, the effective gas diffusivity is also simulated through the 3D CFD simulation. Finally, the compressed GDL geometry profile and simulated gas diffusivity are imported into the 3D CFD multiphase model. The effect of the contact resistance on the cell performance is considered and analyzed. The rest of the paper is organized as follows. Section 2 describes physical and numerical models, including the 3D finite-element analysis (FEA) compression model (brief introduction), 3D gas diffusion model, two-dimensional (2D) FEA deformation model, and 3D CFD multiphase model. Section 3 presents numerical results and discussion. Finally, conclusions are presented in Section 4.

2. Model description

2.1. 3D FEA compression model

Based on geometric assumptions [25], the microstructure of the GDL could be stochastically reconstructed, as shown in Fig. 1(a). The poros-
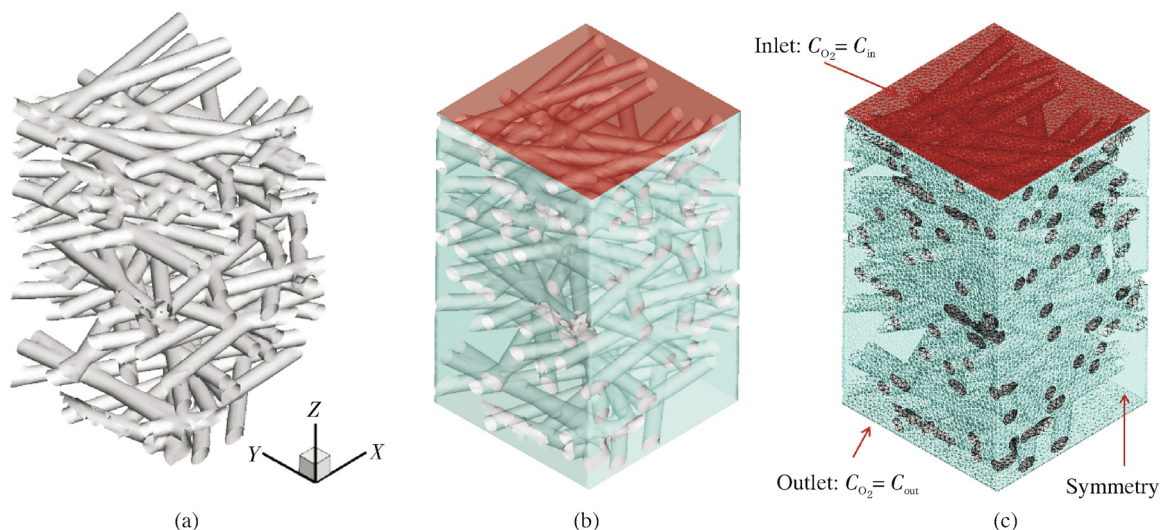
Fig. 2. 3D computational fluid dynamics (CFD) gas diffusion model. (a) Solid fiber; (b) extracted fluid domain; (c) mesh generation and boundary conditions.

Table 1
Parameters in the 3D finite-element analysis (FEA) compression model.

Parameters	Value
Young's modulus of the BP/fiber	13/3 GPa
Poisson ratio of the BP/fiber	0.26/0.256
GDL porosity	0.78
GDL thickness	195 μm
Fiber diameter	9.75 μm
In-plane dimensions (X/Y)	120/120 μm

Note: bipolar plate (BP); gas diffusion layer (GDL).

ity, fiber diameter, and thickness of the GDL are key raw material parameters that have large influences on the compression behavior. The stochastic reconstruction techniques employ random generators to create a numerical porous structure representing the realistic GDL material based on information from the material composition and manufacturing process [26]. In the constructed fiber matrix, the fibers are randomly arranged in the plane and pores with different sizes are formed. The employed stochastic algorithm for the construction of the fiber matrix [13] has been widely used in numerical simulations of the GDL region [27–29]. The relevant model parameters are listed in Table 1. A solid mechanical simulation is then carried out to evaluate the mechanical behavior of the GDL. In this FEA model, one side of the GDL is fixed and a pressure is applied on the other side. All boundary conditions are shown in Fig. 1(b). The compressed microstructure and stress–strain curve can be obtained by the simulation results. The microstructure reconstruction and FEA are described in detail in our previous paper [13].

2.2. 3D gas diffusion model

The 3D computational domain of the gas diffusion model is obtained by the 3D FEA results. Fig. 2(a) shows the compressed microstructure obtained by the 3D FEA compression model. The reactant gas diffuses in the pores. As a result, the fluid domain can be extracted, as shown in Fig. 2(b).

The mass transport of gas is governed by the Fick diffusion law

$$\nabla\left(D_0 \nabla C\right) = 0 \tag{1}$$

where D_0 (m^2·s^{-1}) is the intrinsic gas diffusivity, which can be eliminated with the constant assumption, and C (mol·m^{-3}) is the gas concentration. Eq. (1) can be then simplified to the Laplace equation,

$$\nabla(\nabla C) = 0 \tag{2}$$

The inlet and outlet gas concentrations are fixed, and four side faces are set as symmetry boundaries, as shown in Fig. 2(c). According to the principle that the macro and microdiffusion fluxes are equal, the gas diffusivity correction factor used in the 3D CFD transport model can be obtained by

$$\frac{D_{\text{eff}}}{D_0} = \frac{l(\iint_A \frac{\partial C}{\partial z} dx\, dy)}{A(C_{in} - C_{out})} \tag{3}$$

where D_{eff} is the effective gas diffusivity, A is the outlet area of the 3D gas diffusion model, and l is the thickness of the compressed GDL. The unstructured mesh is employed to discretize the fluid domain, as shown in Fig. 2(c). Fig. 3(a) shows the grid independence results. The average concentration flux on the outlet surface changes slightly when the grid number reaches 3.8 million. Considering the calculation time and accuracy, this grid size is employed here.

2.3. 2D FEA deformation model

The GDL deformation on a millimeter scale is needed to study the cell performance on a typical unit (usually a single straight channel). Because the length of the typical unit (50 mm) in this study is rather larger than the width (1.7 mm) and the force on the GDL does not change along the length or flow direction, the model is simplified as a 2D zone as shown in Fig. 4. It consists of a BP and GDL. Other components are ignored due to the higher Young's module than that of the GDL, and the pressure is applied on the top surface of the BP. The mesh in the contact area between the BP and GDL is dense. Thus, the GDL undergoes a large displacement or deformation, as shown in Fig. 4. A grid independence analysis is carried out, as shown in Fig. 3(b). Accordingly, a 30,205-mesh system is subsequently employed.

Different from using a constant Young's modulus to characterize the GDL's mechanical behavior, in this study, the stress–strain curve of the GDL obtained by the 3D FEA microstructure results [13] is employed, as shown in Fig. 5. It is regarded as a type of plastic material. The data table of the stress–strain curve could be imported.

2.4. 3D CFD multiphase model

A 3D multiphase model is developed to study the effect of the assembly pressure on the cell performance. Fig. 6 shows the computational domain (Fig. 6(a)) and model validation results (Fig. 6(b)). The governing equations are listed in Table 2. Details about the corresponding source term and boundary conditions are presented in Ref. [30].
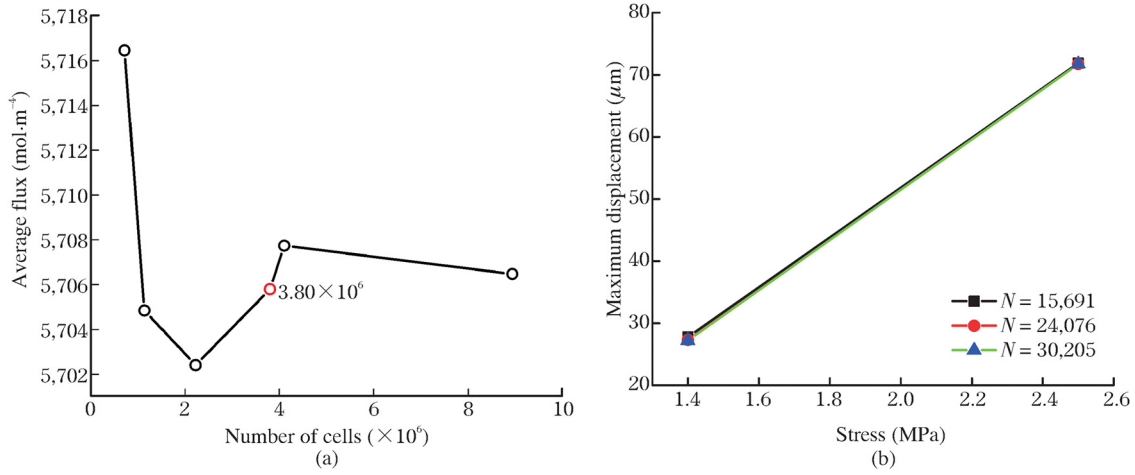
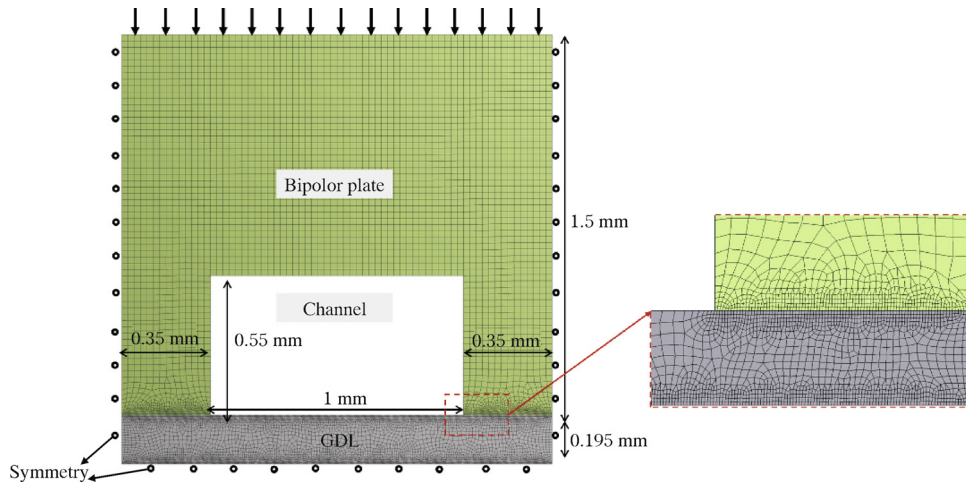**Fig. 3.** Grid independence analysis. (a) 3D gas diffusion model; (b) 2D finite-element analysis (FEA) deformation model.

Fig. 4. 2D finite-element analysis (FEA) deformation model. Gas diffusion layer (GDL).

Table 2
Governing equations of the 3D computational fluid dynamics (CFD) multiphase model.

Solution zone	Physical quantity	Governing equation
GCs, GDLs, MPLs, CLs	Gas density ρ_g	$\nabla \cdot (\rho_g \vec{u}_g) = S_m$
GCs, GDLs, MPLs, CLs	Gas mixture velocity $\vec{u}_g$	$\nabla \cdot (\frac{\rho_g \vec{u}_g \vec{u}_g}{\varepsilon^2(1-s_{lq})^2}) = -\nabla p_g + \mu_g \nabla \cdot (\nabla(\frac{\vec{u}_g}{\varepsilon(1-s_{lq})}) + \nabla(\frac{\vec{u}_g^T}{\varepsilon(1-s_{lq})}))$
		$- \frac{2}{3}\mu_g \nabla(\nabla \cdot (\frac{\vec{u}_g}{\varepsilon(1-s_{lq})})) + S_u$
GCs, GDLs, MPLs, CLs	Mass fraction of species Y_i	$\nabla \cdot (\rho_g \vec{u}_g Y_i) = \nabla \cdot (\rho_g D_i^{eff} \nabla Y_i) + S_i$
BPs, GDLs, MPLs, CLs	Electronic potential ϕ_{ele}	$0 = \nabla \cdot (\kappa_{ele}^{eff} \nabla \phi_{ele}) + S_{ele}$
MEM, CLs	Proton potential ϕ_{ion}	$0 = \nabla \cdot (\kappa_{ion}^{eff} \nabla \phi_{ion}) + S_{ion}$
GDLs, MPLs, CLs	Liquid pressure p_{lq}	$0 = \nabla \cdot (\rho_l \frac{K k_{lq}}{\mu_{lq}} \nabla p_{lq}) + S_{lq}$
MEM, CLs	Membrane water content λ_{mw}	$\nabla \cdot (\frac{n_d}{F} \vec{I}_{ion}) = \frac{\rho_{mem}}{EW} \nabla \cdot (D_{mw}^{eff} \nabla \lambda_{mw}) + S_{mw}$
Whole domain	Temperature T	$\nabla \cdot ((\rho C_p \vec{u})^{eff} T) = \nabla \cdot (k^{eff} \nabla T) + S_E$

Note: gas channel (GC), microporous layer (MPL); catalyst layer (CL); membrane (MEM).

Table 3 lists key parameters that affect the cell performance (polarization curve). They are obtained from a commercial BP and MEA. More details are presented in our previous paper [31]. To validate the model, these parameters are initially set to those in Ref. [32]. The predicted polarization curve agrees with the experiment data, as shown in Fig. 6(b), which validated our model accuracy. As shown in Fig. 6(a), the profile of the deformed GDL obtained from the 2D FEA deformation model is imported into the 3D model. The deformation of the GDL directly leads to a change in the porosity distribution. In the plane perpendicular to the Z axis, the local porosity could be calculated by the local compression by

$$\gamma_{new} = 1 - (1 - \gamma_{original})\frac{\delta_{original}}{\delta_{new}} \tag{4}$$

where γ and δ are the porosity and thickness, respectively.
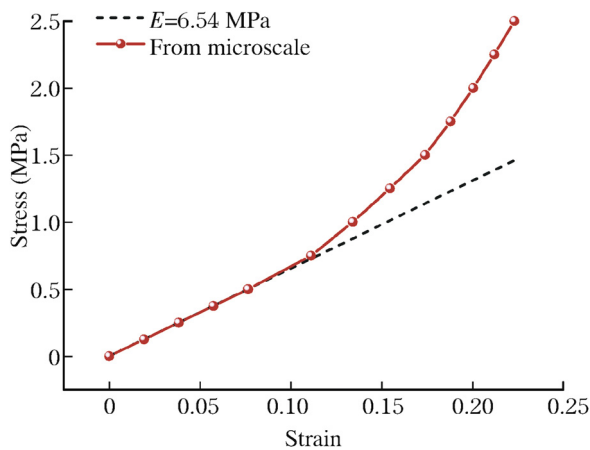
Fig. 5. Stress–strain curve of the gas diffusion layer (GDL) material.
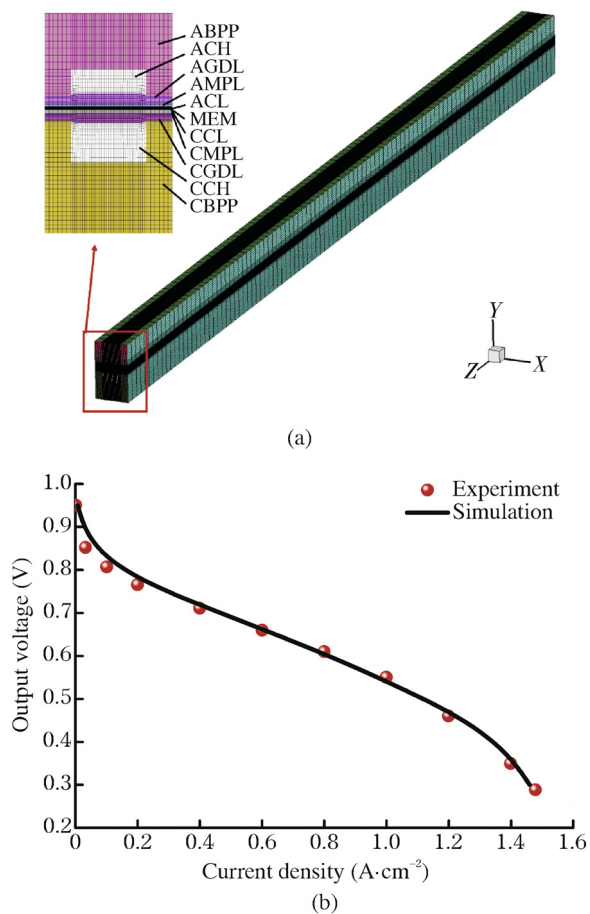

(a)

(b)

Fig. 6. Computational domain validation of the 3D computational fluid dynamics (CFD) multiphase model. (a) Computational domain for the 3D CFD multiphase model; (b) 3D CFD multiphase model validation.

Other porosity-dependent transport properties, such as the permeability, effective conductivity, source term of the gas–liquid phase change, and Leverett J value, also change accordingly. Notably, the correction factor of the effective gas diffusivity in the GDL is obtained by the 3D gas diffusion model rather than using the Bruggemann correction, $\gamma^{1.5}$.

The assembly force significantly changes the electrical contact resistance (ECR) at the BP–GDL interface. The ECR correlation model pro-

Table 3
Key parameters in the 3D CFD model.

Parameters	Value	Unit
Width of rib, channel	1, 0.35	mm
Length of BP	50	mm
Height of channel (anode/cathode)	0.35/0.55	mm
Thicknesses of MPL, ACL, MEM, CCL	45, 6, 15, 18	μm
Density of MEM (ρ_{MEM})	2,150	kg·m^{-3}
Equivalent weight of MEM	1,000	kg·mol^{-1}
Porosities of MPL, CL	0.4, 0.3814	-
Contact angles of GDL, MPL, CL	159, 166, 140	°
Transfer coefficient (anode/cathode)	0.25/0.25	-
Volumetric reference exchange current density (anode/cathode)	12×10^9/758.94	A·m^{-3}
Reference concentration of hydrogen, oxygen	40, 40	mol·m^{-3}
Stoichiometry ratio (anode/cathode)	1.5/1.5	-
Back pressure (anode/cathode)	1.5/1.5	bar
Relative humidity (anode/cathode)	100/100	%
Operating temperature	353.15	K

Note: anode catalyst layer (ACL); cathode catalyst layer (CCL).

posed by Zhou et al. [33] has been employed to estimate the total contact resistance in similar studies [34,35], which is expressed by

$$R_{contact} = \frac{1}{\sum_{i=1}^{n} \frac{1}{R_i}} = \frac{1}{\sum_{i=1}^{n} \frac{S_i}{a(b/p_i)^c}} \tag{5}$$

where $R_{contact}$ is the total ECR, n is the number of contact elements at the interface, S_i is the area of the ith contact element, p_i is the ith contact stress, and a, b, and c are constant coefficients. For the contact of a stainless steel and carbon paper, the coefficients are set to $a = 81.4$ mΩ·cm^2, $b = 2.52$ MPa, and $c = 1.07$ [33].

The average contact pressure is practically constant and independent on the number of cells, 1.4 to 1.6 MPa [4]. The value of 1.4 MPa is recommended by the US Department of Energy for interfacial contact resistance measurements [36]. Besides, the range of 0.5–2.5 MPa is in line with the actual levels demonstrated in similar studies [22,24,37,38]. Therefore, 0.5, 1.4, and 2.5 MPa are chosen as low, medium, and high levels of assembly pressure, respectively.

3. Results and discussion

The results of the 3D FEA compression model are presented in our previous paper [13], and thus they are not repeated here. Based on its compression results, the gas diffusivity and GDL macroscopic deformation profile are illustrated in this section. Furthermore, on a macroscopic scale, the effects of the compression on the cell performance, fluid flow, mass transport, reaction rate, and water and thermal management are analyzed.

3.1. Gas diffusivity after compression

To compare with the experiment data, we evaluate the compression ratio and oxygen diffusivity under three assembly pressures (1.4, 2.5, and 3.0 MPa). Based on the original GDL, the normalized diffusivity after the compression is defined. The simulation and experiment [39] are compared in Fig. 7. The simulation value is close to the experimental value, which verifies the accuracy of the model. Fig. 8 shows the diffusivity correction factor calculated by Eq. (3). The diffusivity correction factors at 1.4 and 2.5 MPa are reduced by approximately 9.97% and 14.43%, respectively, compared with the original GDL (without compression). For comparison, the correction factor calculated by the Bruggemann equation is also plotted. The simulation value f_m is lower than the Bruggemann value f_B, approximately 0.86 times f_B. The diffusivity calculated above is used in the 3D CFD multiphase model.

Table 4
Correlations of porosity-related parameters.

Parameter	Correlation
Permeability (m²) [40]	$\frac{\kappa}{d^2} = \gamma(\frac{\pi^2}{16(1-\gamma)^2} - \frac{\pi}{2(1-\pi)} + 1)(1 + 0.72\frac{1-\gamma}{(\gamma-0.11)^{0.5\pi}})$
Effective electrical conductivity (S·m⁻¹)	$\sigma_{GDL,eff} = (1-\gamma)^{1.5}\sigma_{GDL,s}$
Leverett J value for the capillary pressure	$p_c = \begin{cases} \varpi\cos\theta(\frac{\gamma}{\kappa_0})^{0.5} \times [1.42(1-s_{lq}) - 2.12(1-s_{lq})^2 + 1.26(1-s_{lq})^3]\theta < 90° \\ \varpi\cos\theta(\frac{\gamma}{\kappa_0})^{0.5} \times [1.42s_{lq} - 2.12s_{lq}^2 + 1.26s_{lq}^3]\theta > 90° \end{cases}$
Source term of gas–liquid phase change	$S_{v-l} = \begin{cases} \alpha\gamma(1-s_{lq})(\rho_{vap} - \rho_{sat}), \rho_{vap} > \rho_{sat} \\ \alpha\gamma s_{lq}(\rho_{vap} - \rho_{sat}), \rho_{vap} < \rho_{sat} \end{cases}$

Note: In the Leverett J function, p_c represents the capillary pressure, ϖ is the surface tension coefficient, θ is the contact angle, γ is the porosity, s_{lq} is the liquid water saturation, and κ is the intrinsic permeability.
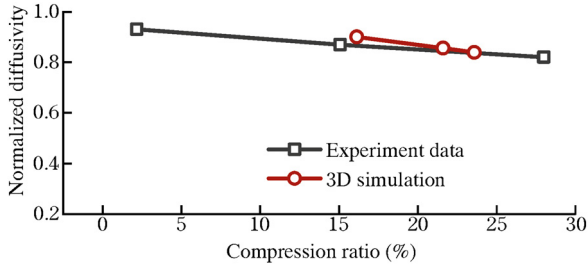

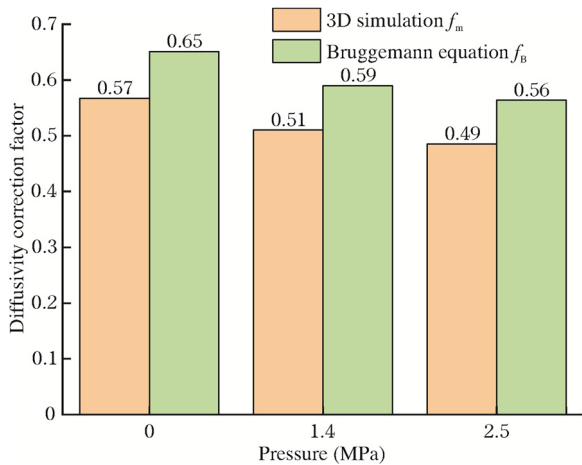**Fig. 7.** Validation of the 3D gas diffusion model.

Fig. 8. Simulation results of the 3D gas diffusion model.

3.2. Data preparation for the 3D CFD multiphase model

Through the 2D FEA deformation model, the geometry profile of the compressed GDL is obtained, as shown in Fig. 9(a). The GDL under the rib is compressed significantly. This cross section is employed to draw the computation domain of the 3D CFD multiphase model.

The correction factor simulated by the 3D gas diffusion model is used for the calculation of the effective gas diffusivity. Fig. 9(b) shows that the cathode oxygen diffusivity is lower than the anode hydrogen diffusivity. Therefore, more attention should be payed to the limitation of cathode mass transfer. Fig. 9(c) shows the distribution of porosity. A common characteristic of the porosity and diffusivity is that they are lower under the rib than under the channel. However, the electrical conductivity distribution is higher under the rib than under the channel. Table 4 [40] lists porosity-related parameter correlations. All of these space distributions are implemented through the user defined function.

3.3. Cell performance prediction

3.3.1. Effect on the cell performance

Fig. 10(a) shows polarization and power density curves under the three assembly pressures when the ECR is not considered. A lower pressure led to a better output performance, particularly under the concentration-dominant zone. The voltage loss analysis in Fig. 10(b) shows that when the assembly force is weaker, the Ohmic loss is large while the activation and concentration losses are small. The compression increases the effective conductivity, thus reducing the Ohmic loss. The output voltage at 2.5 MPa decreases by approximately 15.4% at 1.7 A·cm⁻² compared with that at 0.5 MPa (concentration-dominant zone), owing to the decreases in the porosity and permeability, which largely impacts the mass transfer.

An important role of the assembly pressure is to decrease the ECR between the BP and MEA. The stress distribution at the BP–GDL interface is shown in Fig. 10(c). The stress under the rib is higher than that under the channel. The stress peak appears at the junction of the channel and rib. The ECR could then be calculated by the stress according to Eq. (5). The predicted ECRs are 343.57, 121.20, and 67.61 mΩ at 0.5, 1.4, and 2.5 MPa, respectively.

After the ECR (as a part of the Ohmic impedance) is considered, the polarization and power density curves shift downward, as shown in Fig. 10(d). At current densities lower than 1.7 A·cm⁻², a higher pressure led to a better performance, which is contrary to the case when the contact resistance is not considered, because the lower assembly pressure leads to a large Ohmic impedance. In this study, under a low pressure (0.5 MPa), the contact resistance is dominant in the Ohmic impedance. Therefore, the output voltage decreases largely with the increase in the current density under a pressure of 0.5 MPa. When the assembly pressure increases to medium (1.4 MPa) and high (2.5 MPa) levels, the contact resistance significantly decreases. The mass transport and contact resistance have important contributions to the output performance. When the assembly force is large, the contact resistance is small, which is conducive to an Ohmic loss. However, it deteriorates the mass transfer (by reducing the porosity) and increases the concentration loss. Considering these two aspects, under the Ohmic-dominant zone, the performance at 2.5 MPa is higher than that at 1.4 MPa. The opposite behavior is observed in the concentration-dominant zone (higher than 1.7 A·cm⁻²).

3.3.2. Effect on the fluid flow

To study the effect of the assembly pressure on the gas flow or pressure drop, the change in pressure drop is shown in Fig. 11(a). Fig. 11(b) shows the pressure distributions in the cathode GDL, MPL, and CL at 1.7 A·cm⁻². With the increase in the current density, the pressure drop increases due to the mass flow rate increase. Besides, the compression leads to a significant increase in pressure drop. The pressure drop at 2.5 MPa is 20% higher than that at 1.4 MPa at the same current density of 1.7 A·cm⁻². Owing to the compression, the GDL under the channel is bulged, which reduces the flow cross-section area of the flow channel. The flow velocity becomes larger under the same volume flow rate.
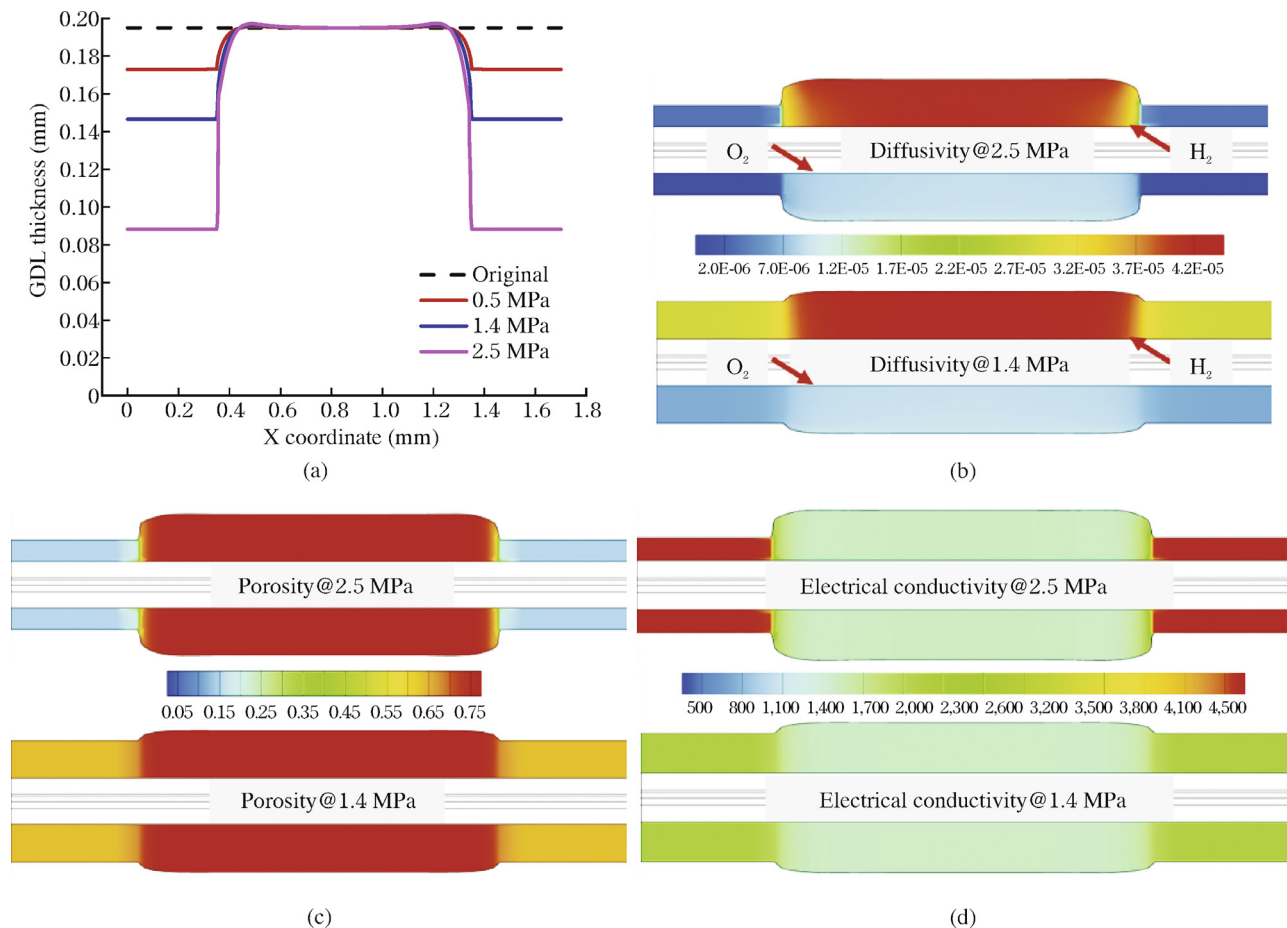
Fig. 9. Data preparation for the 3D multiphase model. (a) GDL compression profile; (b) effective gas diffusivity distribution; (c) porosity distribution; (d) effective electrical conductivity distribution.

However, the compression results in reduced GDL porosity and intrinsic permeability. This implies that the flow resistance for gas flowing into the porous electrode increases. Considering the above two effects, the pressure loss increases considerably.

3.3.3. Effects on the mass transport and reaction

Figs. 12(a) and 12(b) show the O_2 concentration and reaction rate in the CCL under assembly pressures of 1.4 and 2.5 MPa, respectively. O_2 is hard to flow into the region under the rib where the porosity and permeability are lower. The reaction rate and reactant concentration are coupled. In the flow direction, both O_2 concentration and reaction rate decrease from the inlet to the outlet, due to the consumption of the oxygen reduction reaction.

In the vertical direction, the lower O_2 concentration under the rib yields a lower reaction rate under the rib, as shown in Fig. 12(b). Under the same current density (1.7 A·cm^{-2}), the total generated current is the same. As a result, the total reaction intensity (integration of the reaction rate over the whole CCL zone) is unchanged, but the distribution of the reaction rate becomes uneven. In other words, at a higher degree of compression, the chemical reaction is more concentrated under the flow channel, as shown in Fig. 12(c). Furthermore, the higher reaction rate implies a higher flux or higher gradient of O_2 concentration under the channel. According to the isoline distribution, Fig. 12(d) shows that the O_2 concentration decreases faster at 2.5 MPa in the through-plane direction. Generally, at the high-level compression, the reactant concentration in the CL decreases rapidly, and the cell performance enters the concentration-dominant zone faster. This validates the polarization curve results in Figs. 10(a) and 10(d).

3.3.4. Effect on the water and thermal management

Fig. 13(a) shows the temperature distributions in the CCL under the assembly pressures of 1.4 and 2.5 MPa. The distribution characteristics are almost the same as those of the reaction rate shown in Fig. 12(b). A valley-type higher-temperature region occurs in the left center part of the membrane, which can be explained as follows. In this study, the temperatures of the surrounding walls of the cell and inlets in the domain are set as the operating temperature (353.15 K) [30]. The temperature is higher in places with large heat sources. Fig. 12(b) shows that the reaction rate at the cathode inlet is higher, which leads to more irreversible heat of the electrochemical reactions. Therefore, the temperature near the cathode inlet is higher than that near the outlet. The temperature under the rib is lower than that under the channel. This has also been observed in Ref. [41].

For the water distribution, the liquid water saturation profiles are shown in Fig. 13(b). The liquid saturation is obtained from the inverse solution of the capillary pressure by the Leverett J function (listed in Table 4). As the contact angle, porosity, and intrinsic permeability are different in the GDL, MPL, and CL, there is a liquid water saturation jump at the interfaces of different layers, as shown in Fig. 13(b). Besides, the liquid water saturation increases at 2.5 MPa. This demonstrates that the compression also hinders the discharge of liquid water. The membrane water content variation is shown in Fig. 13(c). With the increase in the current density, the membrane water content initially increases, and then decreases, owing to the combined effect of two factors. With the increase in the current density, the temperature increases to promote the conversion of membrane water. However, the content of membrane water produced by the reaction also increases. The membrane water
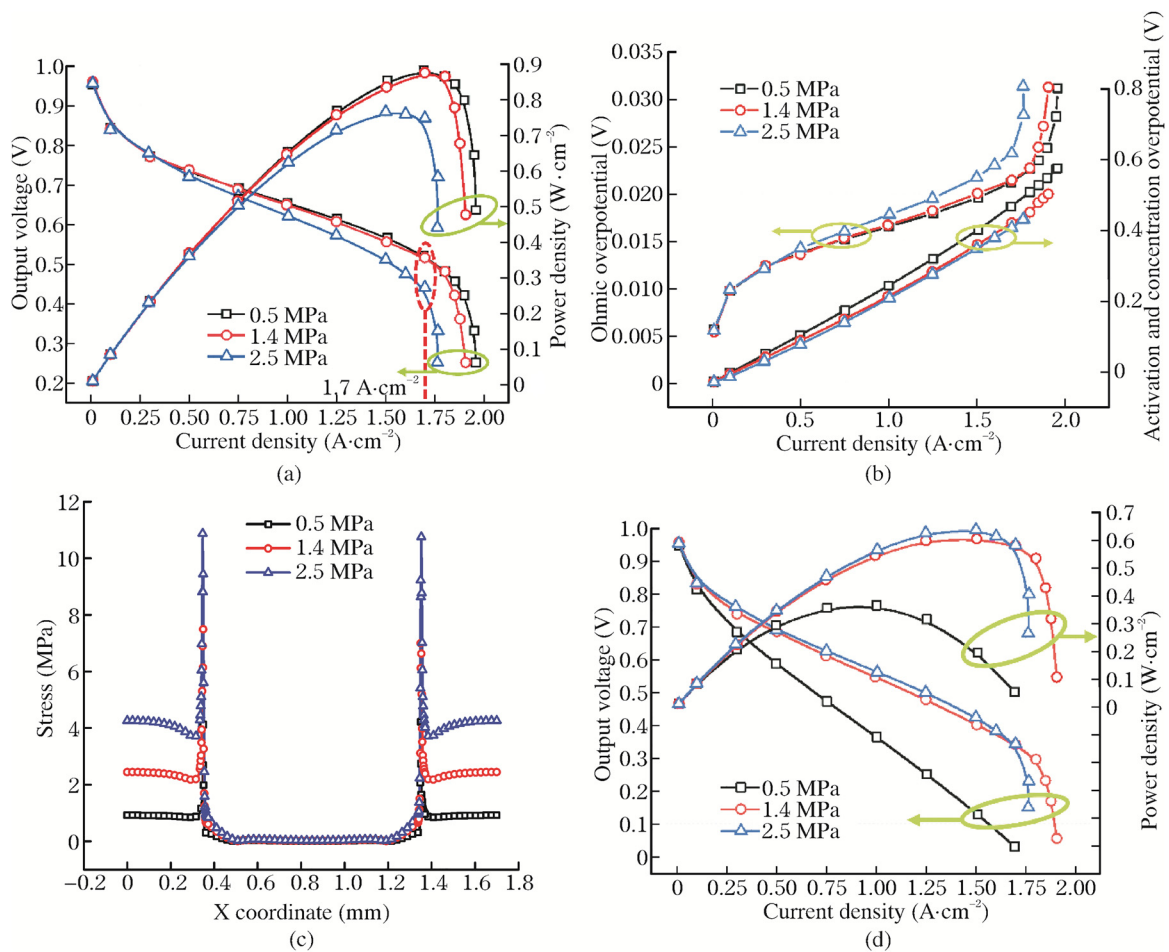
Fig. 10. Cell performance and contact resistance. (a) Without contact resistance; (b) voltage loss; (c) stress distribution; (d) with considered contact resistance.
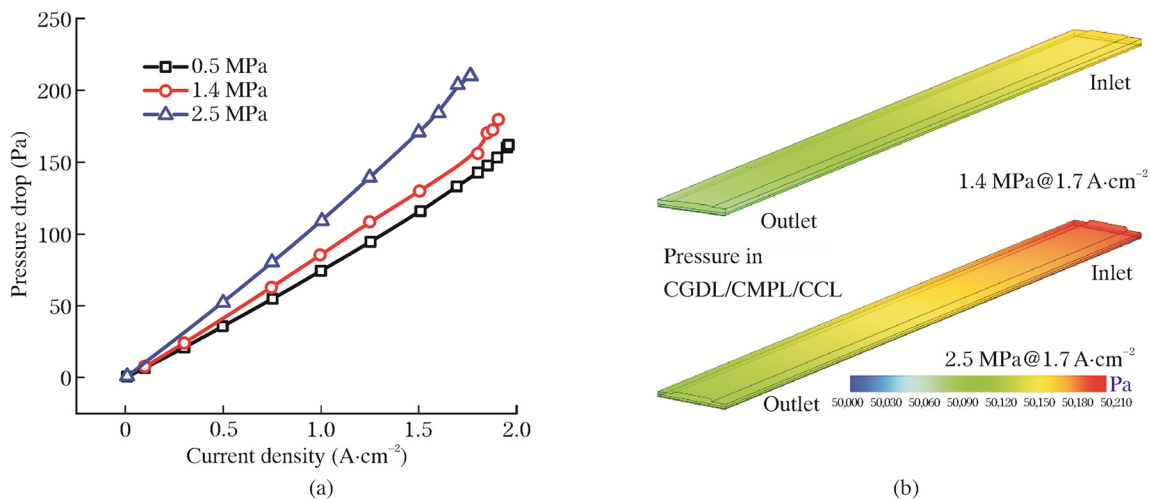

Fig. 11. Effect on the pressure distribution. (a) Pressure drop; (b) pressure contour at 1.7 A·cm⁻². Cathode gas diffusion layer (CGDL); cathode microporous layer (CMPL); cathode catalyst layer (CCL).

content is high when the pressing force is large. A wet membrane implies a smaller proton Ohmic resistance, which is consistent with Fig. 10(b).

4. Conclusion

In this study, based on the microstructure of the compressed GDL, the effective oxygen diffusion coefficient was obtained by a simulation. The deformation GDL profile was obtained by substituting the nonlinear stress–strain law into the 2D FEA deformation model. Finally, the influences of the assembly force on the fluid flow, mass transport, reaction rate, water and thermal management, and fuel cell performance were studied by the 3D CFD multiphase model. The findings of this study can be summarized as follows.

(1) The effective oxygen diffusion coefficient simulated by the compressed GDL is approximately 0.86 times the Bruggemann's estimated value f_B.
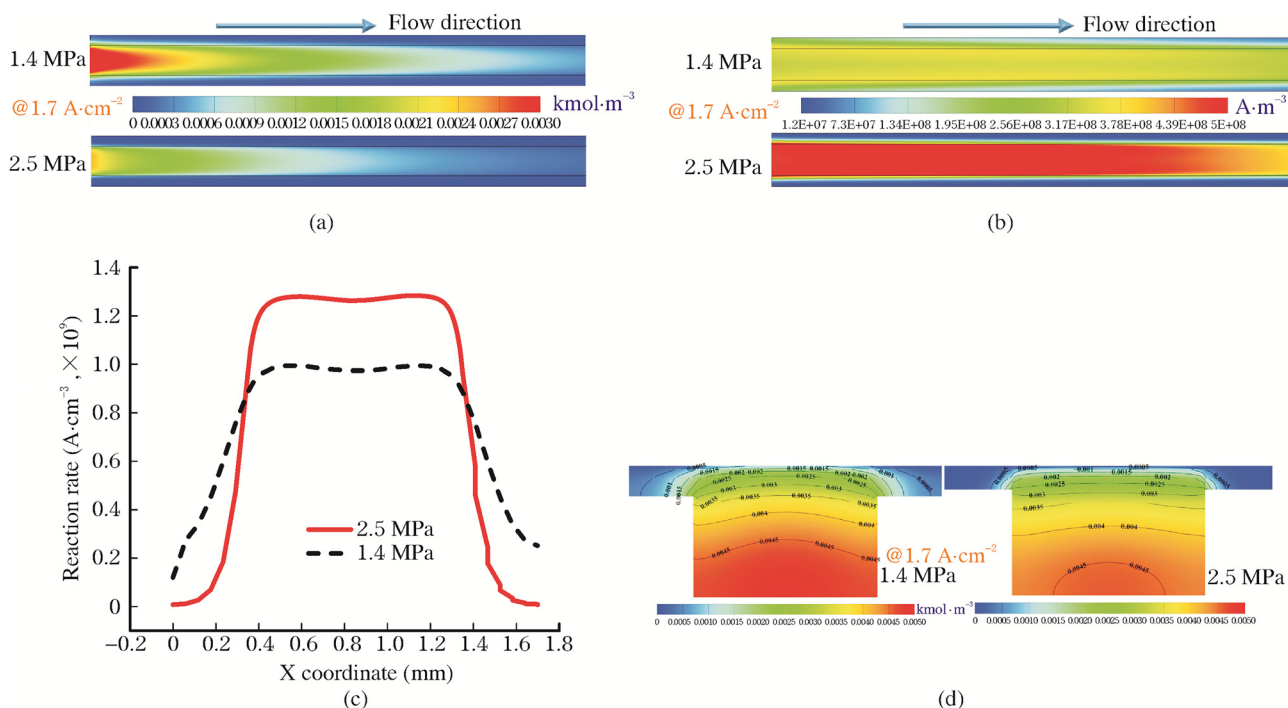
Fig. 12. Cathode reaction rate and O$_2$ concentration distribution in the cathode catalyst layer (CCL). (a) O$_2$ concentration in the CCL; (b) reaction rate in the CCL; (c) average reaction rate in the X direction (rib–channel–rib) in the CCL; (d) O$_2$ concentration in the cross-section plane.
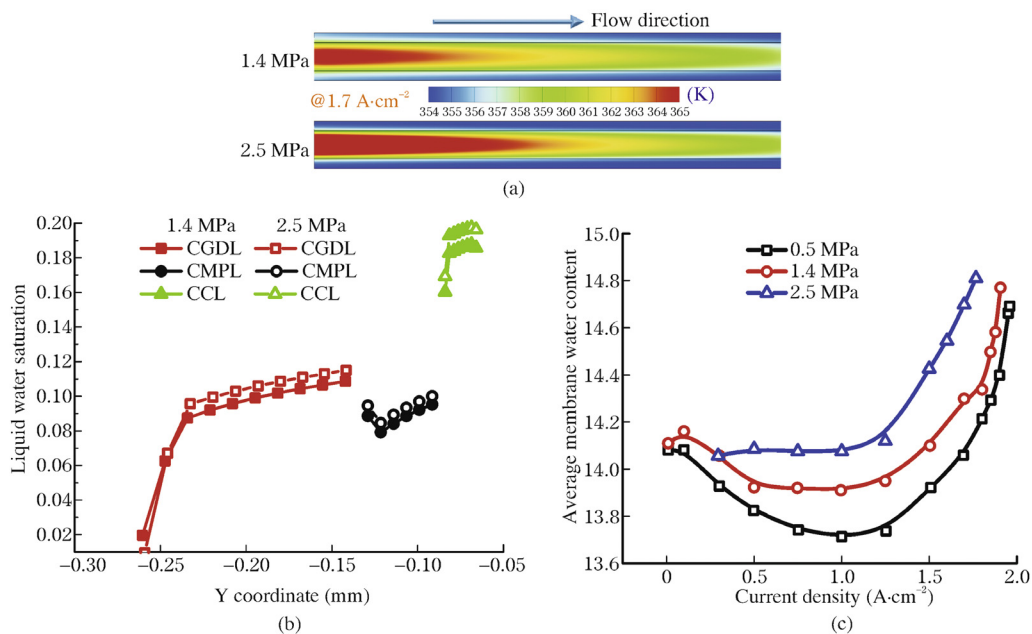

Fig. 13. Temperature and water distributions at 1.7 A·cm^{-2}. (a) Temperature distribution in the membrane (MEM); (b) liquid water saturation distribution in the cathode in the through-plane direction; (c) membrane water content.

(2) The compression has significant effects on both contact resistance and mass transport ability. The contact resistance has an important role under the Ohmic-dominant zone. As a result, the cell performance at 2.5 MPa with the small contact resistance was better than that at 1.4 MPa with the large contact resistance. However, the opposite behavior was obtained in the concentration-dominant zone (higher than 1.7 A·cm^{-2}), where the mass transfer deterioration became the main reason for the performance degradation.

(3) The GDL porosity and permeability decrease after the compression. The pressure drop of the 2.5 MPa case was 20% higher than that of the 1.4 MPa case at 1.7 A·cm^{-2}. O$_2$ was hard to flow into the region under the rib where the porosity and permeability were lower.

(4) The reaction rate was lower under the rib due to the lower O$_2$ concentration. Furthermore, this uneven distribution became more obvious with the increase in the assembly force.

(5) Both liquid water and membrane water contents increased when the assembly force increased. A wet membrane implies a smaller proton Ohmic resistance.

Declaration of Competing Interest

The authors declare that there are no conflicts of interest.

Acknowledgments

CRediT author statement

Zhuo Zhang: Conceptualization, Methodology, Software, Writing-Original draft preparation. **Wen-Quan Tao**: Writing-Reviewing and Editing, Supervision.

References

[1] F. Bai, L. Lei, Z. Zhang, et al., Application of similarity theory in the study of proton exchange membrane fuel cells: a comprehensive review of recent developments and future research requirements, Energy Storage Sav. 1 (2022) 3–21.

[2] Z. Zhang, J. Shi, X. Cheng, et al., Numerical examination of high-pressure fuel injection in common rail injector based on hydro-mechanical model, Phys. Fluids 34 (2022) 057114.

[3] G. Zhang, L. Wu, Z. Qin, et al., A comprehensive three-dimensional model coupling channel multi-phase flow and electrochemical reactions in proton exchange membrane fuel cell, Adv. Appl. Energy 2 (2021) 100033.

[4] C. Carral, P. Mélé, A numerical analysis of PEMFC stack assembly through a 3D finite element model, Int. J. Hydrog. Energy 39 (2014) 4516–4530.

[5] A.M. Dafalla, F. Jiang, Stresses and their impacts on proton exchange membrane fuel cells: a review, Int. J. Hydrog. Energy 43 (2018) 2327–2348.

[6] C.-Y. Chen, S.-C. Su, Effects of assembly torque on a proton exchange membrane fuel cell with stamped metallic bipolar plates, Energy 159 (2018) 440–447.

[7] M.S. Ismail, A. Hassanpour, D.B. Ingham, et al., On the compressibility of gas diffusion layers in proton exchange membrane fuel cells, Fuel Cells 12 (2012) 391–397.

[8] N. Keller, P. Hübner, T. von Unwerth, Investigation of intrusion effects of a gas diffusion layer into channel cross sections depending on channel parameters of metallic bipolar plates, Int. J. Hydrog. Energy 45 (2020) 15366–15379.

[9] K.D. Baik, B.K. Hong, K. Han, et al., Correlation between anisotropic bending stiffness of GDL and land/channel width ratio of polymer electrolyte membrane fuel cells, Int. J. Hydrog. Energy 37 (2012) 11921–11933.

[10] C. Carral, P. Mélé, A constitutive law to predict the compression of gas diffusion layers, Int. J. Hydrog. Energy 43 (2018) 19721–19729.

[11] M.F. Serincan, U. Pasaogullari, Effect of gas diffusion layer anisotropy on mechanical stresses in a polymer electrolyte membrane, J. Power Sources 196 (2011) 1314–1320.

[12] Z. Lu, C. Kim, A.M. Karlsson, et al., Effect of gas diffusion layer modulus and land—groove geometry on membrane stresses in proton exchange membrane fuel cells, J. Power Sources 196 (2011) 4646–4654.

[13] Z. Zhang, P. He, Y.-J. Dai, et al., Study of the mechanical behavior of paper-type GDL in PEMFC based on microstructure morphology, Int. J. Hydrog. Energy 45 (2020) 29379–29394.

[14] D. Froning, J. Yu, G. Gaiselmann, et al., Impact of compression on gas transport in non-woven gas diffusion layers of high temperature polymer electrolyte fuel cells, J. Power Sources 318 (2016) 26–34.

[15] Y. Xu, D. Qiu, P. Yi, et al., An integrated model of the water transport in nonuniform compressed gas diffusion layers for PEMFC, Int. J. Hydrog. Energy 44 (2019) 13777–13785.

[16] L. Holzer, O. Pecho, J. Schumacher, et al., Microstructure-property relationships in a gas diffusion layer (GDL) for polymer electrolyte fuel cells, part i: effect of compression and anisotropy of dry GDL, Electrochim. Acta 227 (2017) 419–434.

[17] P.R. Chowdhury, A. Vikram, R.K. Phillips, et al., Measurement of effective bulk and contact resistance of gas diffusion layer under inhomogeneous compression – part II: thermal conductivity, J. Power Sources 320 (2016) 222–230.

[18] E. Sadeghi, N. Djilali, M. Bahrami, Effective thermal conductivity and thermal contact resistance of gas diffusion layers in proton exchange membrane fuel cells. Part 1: effect of compressive load, J. Power Sources 196 (2011) 246–254.

[19] D. Qiu, H. Janßen, L. Peng, et al., Electrical resistance and microstructure of typical gas diffusion layers for proton exchange membrane fuel cell under compression, Appl. Energy 231 (2018) 127–137.

[20] A. Uzundurukan, M. Bilgili, Y. Devrim, Examination of compression effects on PEMFC performance by numerical and experimental analyses, Int. J. Hydrog. Energy (2020) 35085–35096.

[21] S.A. Atyabi, E. Afshari, S. Wongwises, et al., Effects of assembly pressure on PEM fuel cell performance by taking into accounts electrical and thermal contact resistances, Energy 179 (2019) 490–501.

[22] X. Yan, C. Lin, Z. Zheng, et al., Effect of clamping pressure on liquid-cooled PEMFC stack performance considering inhomogeneous gas diffusion layer compression, Appl. Energy 258 (2020) 114073.

[23] W.Z. Li, W.W. Yang, W.Y. Zhang, et al., Three-dimensional modeling of a PEMFC with serpentine flow field incorporating the impacts of electrode inhomogeneous compression deformation, Int. J. Hydrog. Energy 44 (2019) 22194–22209.

[24] H. Zhang, M.A. Rahman, F. Mojica, et al., A comprehensive two-phase proton exchange membrane fuel cell model coupled with anisotropic properties and mechanical deformation of the gas diffusion layer, Electrochim. Acta 382 (2021) 138273.

[25] J. Hinebaugh, A. Bazylak, Stochastic modeling of polymer electrolyte membrane fuel cell gas diffusion layers – part 1: physical characterization, Int. J. Hydrog. Energy 42 (2017) 15861–15871.

[26] D.M. Fadzillah, M.I. Rosli, M.Z.M. Talib, et al., Review on microstructure modelling of a gas diffusion layer for proton exchange membrane fuel cells, Renew. Sustain. Energy Rev. 77 (2017) 1001–1009.

[27] M.M. Daino, S.G. Kandlikar, 3D phase-differentiated GDL microstructure generation with binder and PTFE distributions, Int. J. Hydrog. Energy 37 (2012) 5180–5189.

[28] L. Hao, P. Cheng, Pore-scale simulations on relative permeabilities of porous media by lattice Boltzmann method, Int. J. Heat Mass Transf. 53 (2010) 1908–1913.

[29] L. Zhu, H. Zhang, L. Xiao, et al., Pore-scale modeling of gas diffusion layers: effects of compression on transport properties, J. Power Sources 496 (2021) 229822.

[30] P. He, Y.-.T. Mu, J.W. Park, et al., Modeling of the effects of cathode catalyst layer design parameters on performance of polymer electrolyte membrane fuel cell, Appl. Energy 277 (2020) 115555.

[31] Z. Zhang, Q.-Y. Wang, F. Bai, et al., Performance simulation and key parameters in-plane distribution analysis of a commercial-size PEMFC, Energy 263 (2023) 125897.

[32] D.N. Ozen, B. Timurkutluk, K. Altinisik, Effects of operation temperature and reactant gas humidity levels on performance of PEM fuel cells, Renew. Sustain. Energy Rev. 59 (2016) 1298–1306.

[33] P. Zhou, C.W. Wu, G.J. Ma, Contact resistance prediction and structure optimization of bipolar plates, J. Power Sources 159 (2006) 1115–1122.

[34] Y. Wang, X. Wang, Y. Fan, et al., Numerical investigation of tapered flow field configurations for enhanced polymer electrolyte membrane fuel cell performance, Appl. Energy 306 (2022) 118021.

[35] N. Keller, T. von Unwerth, Advanced parametric model for analysis of the influence of channel cross section dimensions and clamping pressure on current density distribution in PEMFC, Appl. Energy 307 (2022) 118132.

[36] US Department Of Energy (DOE)Technical Plan-Fuel Cell, US Department Of Energy (DOE), 2011.

[37] Y. Zhou, K. Jiao, Q. Du, et al., Gas diffusion layer deformation and its effect on the transport characteristics and performance of proton exchange membrane fuel cell, Int. J. Hydrog. Energy 38 (2013) 12891–12903.

[38] M. Movahedi, A. Ramiar, A.A. Ranjber, 3D numerical investigation of clamping pressure effect on the performance of proton exchange membrane fuel cell with interdigitated flow field, Energy 142 (2018) 617–632.

[39] L. Xiao, L. Zhu, C. Clökler, et al., Experimental validation of pore-scale models for gas diffusion layers, J. Power Sources 536 (2022) 231515.

[40] A. Tamayol, F. McGregor, M. Bahrami, Single phase through-plane permeability of carbon paper gas diffusion layers, J. Power Sources 204 (2012) 94–99.

[41] S. Toghyani, F. Moradi Nafchi, E. Afshari, et al., Thermal and electrochemical performance analysis of a proton exchange membrane fuel cell under assembly pressure on gas diffusion layer, Int. J. Hydrog. Energy 43 (2018) 4534–4545.